Role of Oxygen Vacancy Defects in the Electrocatalytic Activity of Substoichiometric Molybdenum Oxide

Journal:	*The Journal of Physical Chemistry*
Manuscript ID	jp-2018-03536f.R1
Manuscript Type:	Article
Date Submitted by the Author:	04-Jul-2018
Complete List of Authors:	Kashfi-Sadabad, Raana; University of Connecticut, Institute of Materials Science Yazdani, Sajad; University of Connecticut, Department of Mechanical Engineering Doan Huan, Tran; University of Connecticut, Department of Materials Science and Engineering Cai, Zhao; Yale University, Department of Chemistry Pettes, Michael; Los Alamos National Laboratory, Materials Physics and Applications, Center for Integrated Nanotechnologies; University of Connecticut, Department of Mechanical Engineering and Institute of Materials Science

Role of Oxygen Vacancy Defects in the Electrocatalytic Activity of Substoichiometric Molybdenum Oxide

Raana Kashfi-Sadabad,[a,†] *Sajad Yazdani,*[b,†] *Tran Doan Huan,*[a,c,d] *Zhao Cai,*[e] *and Michael Thompson Pettes*[a,b,f,]*

[a] Institute of Materials Science, University of Connecticut, Storrs, Connecticut 06269, USA.

[b] Department of Mechanical Engineering, University of Connecticut, Storrs, Connecticut 06269, USA.

[c] Department of Materials Science and Engineering, University of Connecticut, Storrs, Connecticut 06269, USA.

[d] Faculty of Applied Sciences, Ton Duc Thang University, Ho Chi Minh City, Vietnam

[e] Department of Chemistry, Yale University, New Haven, Connecticut 06520, USA.

[f] Center for Integrated Nanotechnologies (CINT), Materials Physics and Applications Division, Los Alamos National Laboratory, Los Alamos, New Mexico 87545, USA.

[†] These authors contributed equally to this work.

* Author to whom correspondence should be addressed, email: pettesmt@lanl.gov

Abstract

Mesoporous α-MoO_{3-x} combined with poly (diallyldimethylammonium chloride)-functionalized reduced graphene oxide (PDDA-rGO) are introduced as an inexpensive and efficient oxygen reduction reaction (ORR) catalyst. The mesoporous catalysts are wrapped by conductive rGO sheets via an electrostatic interaction induced by PDDA polyelectrolyte. Thermal interaction of PDDA with MoO_3 efficiently reduces the metal oxide to MoO_{3-x} at 400-600°C creating surface oxygen vacancy. Through a combination of density functional theory (DFT) and experiments, the role of the surface oxygen vacancy sites in the ORR activity of MoO_{3-x} is identified. For the first time, all the energy barriers opposing ORR are calculated at each step for MoO_3 with no oxygen vacancies and MoO_{3-x} with surface oxygen vacancies. It is shown that presence of a Mo^{4+}-$v_O^{\cdot\cdot}$ oxygen vacancy site on the surface significantly reduces the energy barriers against ORR in the reaction pathways. An overpotential of 0.86 V (vs. RHE) with excellent

electrochemical stability was obtained with the newly designed catalyst, with only a 9% decrease in activity after ~17 hours. These results offer a new paradigm in defect engineering of metal oxides with a potential for the synthesis of stable and active noble metal-free ORR electrocatalysts.

Introduction

The oxygen reduction reaction (ORR) is central to the development of various electrochemical systems for energy conversion applications[1]. Developing highly efficient catalysts for ORR is of particular significance in the fabrication of commercial fuel cell devices and metal–air batteries[2]. One of the main challenges in the development of such devices with acceptable cost-effective and energy-efficient characteristics is to find an ideal electrocatalyst for oxygen reduction at the cathode[1]. Nevertheless, electrocatalytic control of the reduction process for gas-phase oxygen is still limited due to slow ORR kinetics which, in turn, is caused by difficult absorption, bond activation, bond cleavage, and removal of oxygen at the solid-gas interface[1]. The slow kinetics of ORR can be overcome through the use of precious noble metal-based catalysts, particularly Pt, which increases the cost significantly. Numerous studies have been conducted on Pt-free catalysts such as transition metal oxides, chalcogenides, nitrides, and oxynitrides[3, 4]. However, the catalytic activity and durability of the existing 'beyond platinum' ORR catalysts are not adequate to an extent that would allow them to replace Pt-based catalysts.

The unique properties of molybdenum-based oxides such as relatively high electrical conductivity and mechanical and thermal durability make them ideal candidates for development of efficient electrochemical energy storage systems[3]. Among different Mo-based electrocatalysts, layered orthorhombic MoO_3 and conductive monoclinic MoO_2 are the most promising[3, 5]. The majority of previous studies on these materials have been carried out in the fields of Li-ion batteries[6], supercapacitors[7, 8], and the hydrogen evolution reaction[6]. However, the main objective of current work is to expand the unique features of Mo-based metal oxides to ORR applications. To the best of our knowledge, only one study has discussed the ORR activity of a MoO_3 which has been conducted on a non-layered hexagonal structure[8].

ORR is a reaction that mainly occurs on the surface of the catalyst due to limited oxygen diffusion into the bulk material. As a result, any effort for an improvement should be achievable by modification of the surface chemistry. Liang and Müllen *et al.*[9] reported a collection of mesoporous metal-based ORR catalysts including cobalt/iron–nitrogen-doped carbon by employing vitamin B_{12} and polyaniline–Fe complexes as precursors. The high ORR activity of the mesoporous catalysts was attributed to their high surface area, and uniform distribution of

metal and nitrogen active spots. A high surface area ensures the maximum oxygen accessibility to the catalyst. The electrical conductivity is another factor that plays a crucial role in the ORR activity of catalysts. Graphene supported metal-based catalysts are one of the most effective means to significantly improve the mechanical and electrical properties as well as surface area[7, 10-12]. Recently, we reported that a thermochemical reaction between PDDA polyelectrolyte and MoO_3 can induce large quantities of oxygen vacancy sites in the metal oxide[13]. It was observed that with a thermal annealing of α-MoO_3 at 600°C under Ar with no PDDA, only a small sub-stoichiometry value of $x \sim 0.03$ was obtained. In contrast, with the use of PDDA, $x = 0.36$ and $x = 0.98$ were obtained for the samples annealed at 600°C under Ar and H_2-containing gas (5%H_2/95%Ar), respectively. This emphasized the effectiveness of PDDA polyelectrolyte in creating high densities of oxygen vacancies in addition to inducing the electrostatic charges useful for wrapping of the active material with conductive supports such as rGO.

Here, reduced graphene oxide (rGO) was used as the conductive support and current collector for the mesoporous catalysts. To have the maximum effectiveness, the samples in our work were made mesoporous with surface areas greater than 50 m^2g^{-1}. We combine mesoporous MoO_3 with rGO into a single composite without spoiling the porous mesostructure. Poly(diallyldimethylammonium chloride) (PDDA) was used to create a strong interaction between the rGO support and mesoporous catalysts, as it induces positive charges on rGO[12] causing a strong electrostatic attraction towards mesoporous MoO_3 samples with negative charges. Additionally, a comprehensive computational study was also performed to fully understand the effects of surface oxygen vacancy sites on the ORR activity of MoO_{3-x}. The results of our DFT calculations supported by experimental observations indicated that the presence of a Mo^{4+}-$v_O^{\cdot\cdot}$ oxygen vacancy site can greatly facilitate the reactions by lowering the corresponding energy barriers.

Experimental section

Chemicals. All chemicals were used as received. Pluronic P123 triblock poly(ethylene oxide)-*b*-poly(propylene oxide)-*b*-poly(ethylene oxide) copolymer (M_w = 5800, $EO_{20}PO_{70}EO_{20}$), 1-butanol (anhydrous, 99.8%), tetraethyl orthosilicate (TEOS), hydrochloric acid (HCl, 37% aqueous), ethyl alcohol (CH_3CH_2OH), phosphomolybdic acid (PMA, $H_3PMo_{12}O_{40}\cdot xH_2O$),

poly(diallyldimethylammonium chloride) (PDDA), potassium permanganate ($KMnO_4$), hydrogen peroxide (H_2O_2, 30%), graphite flakes, and sodium nitrate ($NaNO_3$) were purchased from Sigma-Aldrich Co. LLC.

Synthesis of mesoporous MoO_3 electrocatalysts. In accordance with established procedures[14, 15], mesoporous silica SBA-15 and KIT-6 hard templates were prepared over the period of 24 hours under hydrothermal conditions at a temperature of 100°C. A solvent evaporation induced impregnation process[16, 17] was used to incorporate the PMA precursor into the channels of mesoporous silica similar to the common practice in nanocasting processes. 4.4 g of PMA powder were dispersed in 25g of ethanol followed by the addition of 1 g of SBA-15 template to the solution. The mixture was then stirred intensively at room temperature (20–30°C) for 3 h, before transferring it to a petri dish to be dried at 60°C for 12 h until all of the ethanol evaporated. The obtained PMA/mesoporous silica powder (denoted as PMA@SBA-15) was then transferred into a crucible, heated to 550°C at the rate of 1°C/min, and kept in those conditions for 4 h, producing a MoO_3/mesoporous silica powder (denoted as MoO_3@SBA-15). The silica SBA-15 template in the MoO_3@SBA-15 composite was removed by etching in hydrofluoric acid (4%, aqueous solution). While it may be possible that a small quantity of molybdenum oxide is dissolved in HF, our observation was that MoO_3 was stable in 4% HF aqueous solutions for a period of more than 6 hours. A similar procedure was used to prepare ordered mesoporous MoO_3@KIT-6 samples, except that the SBA-15 template was replaced with an equal amount of KIT-6. The resultant silica template-free powders of MoO_3 nanocast from KIT-6 and SBA-15 are denoted as MoO_3–KIT-6 and MoO_3–SBA-15, respectively.

Synthesis of graphene-wrapped MoO_3–SBA-15. A modified Hummers' method[18, 19] with a lower concentration of oxidizing agent was used to synthesize graphene oxide. The rGO/MoO_3–SBA-15 composite (denoted rGMS) was obtained via an electrostatic interaction between poly (diallyldimethylammonium chloride) (PDDA)-modified graphene oxide and metal oxides in aqueous solutions. In accordance with the procedure described by Chang *et al.*[20], 0.1 mL of a 20 wt% PDDA solution was first mixed into 40 mL of graphene oxide solution with concentration of 0.5 mL/mg and the mixture was sonicated for 1 h until a transparent solution was obtained. After diluting the solution to 100 mL, 200 mg of mesoporous MoO_3–SBA-15 was sonicated into 100 mL of ethanol. Then, the mesoporous MoO_3–SBA-15 solution (negatively charged) was

mixed with 100 mL of graphene oxide solution (positively charged) and stirred for 12 h. After filtering and drying, the as-prepared GO/MoO_3–SBA-15 composite was thermally reduced at 400°C and 600°C with a rate of 1 °C/min and kept for 2 h at these temperatures in an Ar. Finally, the black-colored products of the reduced samples were obtained. Because MoO_3 is partially reduced during the annealing process, the abbreviation MoO_{3-x} is used to refer to the mixed-phase composites. The products rGO/MoO_{3-x}–SBA15-400°C and rGO/MoO_{3-x}–SBA15-600°C are subsequently denoted as rGMS-400 and rGMS-600.

Characterization. Powder X-ray diffraction (XRD) analysis was performed on a Rigaku Ultima IV diffractometer with Cu Kα radiation (λ = 1.5406 Å), with an operating current of 44 mA and voltage of 40 kV, and a Bruker D2 Phaser with Cu K_α radiation (λ = 1.54184 Å) with an operating voltage and current of 30 kV and 10 mA at room temperature. Nitrogen adsorption-desorption isotherms were obtained at -196°C on a Micrometrics ASAP 2010 instrument. Samples were first degassed at 150°C in a vacuum for 6 h. The specific surface areas were derived from adsorption data by the Brunauer–Emmett–Teller (BET) method. The pore-size distributions of the samples were retrieved from the adsorption curves of isotherms by using the Barrett–Joyner–Halenda (BJH) method. The total pore volumes were calculated using the adsorbed volumes at a pressure of P/P_0 = 0.99. Transmission electron microscopy (TEM) analysis was conducted using a FEI Talos F200X TEM/STEM and JEOL 2010 FasTEM both at an accelerating voltage of 200 kV, and chemical analysis was collected using energy dispersive X-ray spectroscopy (EDS). The TEM samples were sonicated in ethanol and collected using thin carbon films covered copper grids. Morphologies of the samples were investigated using field emission scanning electron microscopy (SEM) on a FEI Nova Nano SEM 450 with accelerating voltage of 2.0 kV.

Electrochemical measurements. The electrochemical measurements were carried out at room temperature in a three-electrode glass cell connected to a CH Instruments 760E electrochemistry workstation. A graphite rod was used as the counter electrode and a saturated calomel electrode (SCE) was used as the reference electrode. The potential was calibrated with respect to a reversible hydrogen electrode (RHE) by experimental measurements using two Pt electrodes and working and counter electrodes in a hydrogen-saturated solution. To prepare the working electrode, 4 mg catalyst, 1 mg carbon black, 200 uL ethanol, 800 uL DI-water and 50 uL nafion

solutions were mixed and ultrasonicated for at least 1 h to form a homogeneous catalyst ink. Afterward, 10 μL of this ink was drop-cast onto the 5 mm-diameter glassy carbon rotating disk electrode (RDE, Pine Instruments) and dried under an infrared lamp for 30 min, yielding a catalyst loading of ~0.255 mg/cm^2. Before the test measurements, O_2 was bubbled through the electrolyte solution to supply enough O_2 reactant. Cyclic voltammetry was firstly conducted for tens of scans with a scan rate of 50 mV/s to reach a stable state, and linear sweep voltammetry (polarization curve) with a scan rate of 5 mV/s was measured in 0.1 M KOH electrolyte. AC impedance measurements were carried out in the same configuration at the potential of 1.71 versus RHE from 0.1–10^5 Hz with an AC voltage of 5 mV.

Density functional theory calculations. The density functional theory (DFT) calculations were performed using Vienna Ab initio Simulation Package[21], by employing a basis set of plane waves with kinetic energies up to 500 eV. For all calculations, the Perdew-Burke-Ernzerhof functional[22] was adopted for exchange-correlation energies. Equilibrium structures were assumed when the atomic forces calculated during the optimization fall below 0.01 eV/Å. Following ref. 23, Dudarev's approach[24] was employed to describe the *d* and *f* electrons of Mo, using $U = 6.0$ eV for the onsite Coulomb term. The dispersion van der Waals interaction was calculated using the optB88-vdW functional. For the polaron (Mo^{4+}), we followed the procedure introduced in ref. 25 by intentionally localizing/delocalizing the electron density at the particular Mo sites of interest. For MoO_3 slabs, we appended a vacuum layer of 10 Å thickness to the bulk models, uncovering the O_t atoms on the (010) surface, and suppressing the interaction along the *y* direction. Because of its layered structure, this is the most stable surface of MoO_3. Reaction with PDDA was assumed to occur on this surface.

Results and Discussion

Chemical and structural analyses. Possessing a high surface area can guarantee the access of oxygen to the catalyst while also favoring formation of more vacancy sites on the surface. Mesoporous molybdenum oxide-graphene composites were synthesized using the method described in the experimental section. In the first step, mesoporous MoO_3 was synthesized via a nanocasting technique where SBA-15 and KIT-6 mesoporous silica were used to template cylindrical and gyroidal structures, respectively. After synthesis of mesoporous SBA-15 and

KIT-6, phosphomolybdic acid (PMA, $H_3PMo_{12}O_{40}$) was used as the molybdenum precursor, and was impregnated inside the porous structure of mesoporous silica templates. The choice of precursor in this technique is of the utmost importance; PMA provides required hydrogen-bond interactions with silica templates and it has both a high molybdenum content and high solubility in ethanol, which was used as the solvent. After solvent evaporation, composites of PMA@SBA-15 and PMA@KIT-6 were calcined at 550°C to decompose the PMA into crystalline MoO_3 inside the channels of SBA-15 or KIT-6 templates. The silica templates were removed by etching in a 4% hydrogen fluoride (HF) aqueous solution. Figure 1 shows the low-angle X-ray diffraction (XRD) patterns the SBA-15 and KIT-6 derived mesoporous molybdenum oxide samples. For the SBA-15-based samples (Figure 1a), four distinct peaks are observed which can be assigned to the (100), (110), (200), and (210) Bragg reflections of the P6mm hexagonal structure as per ref. 9. The low-angle XRD of KIT-6 (Figure 1b) shows peaks attributed to the (211), (220), and (321) Bragg reflections of the bicontinuous cubic gyroidal Ia3d structure (Figure 1b), indicating highly ordered mesostructures as per ref. 26. The low-angle XRD patterns of the mesoporous MoO_3@KIT-6 and MoO_3@SBA-15 prepared at 550°C show one intense peak at $2\theta = 1.0°$, corresponding to the poorly resolved (211) and (100) diffraction peaks of SBA-15 and KIT-6, respectively. After removing the template by HF, three well-resolved diffraction peaks were observed from the low-angle XRD pattern of MoO_3–SBA-15, which can be indexed to (100), (110), and (200) diffraction planes of a highly ordered 2D hexagonal structure. This, in turn, indicated that the MoO_3 crystal nanoarrays replicated the ordered mesostructure of their host silica template. In comparison, after removal of silica with HF, the MoO_3–KIT-6 sample only exhibited one intense peak at $2\theta = 0.9°$ [assigned to (211)], indicating lower structural regularity (see Figure 1b). Further details on the low-angle diffraction patterns of the samples is discussed in the supporting information. As shown in Figure 2, peaks in the high-angle XRD patterns of the mesoporous sample after removing SBA-15 and KIT-6, denoted as MoO_3–SBA15 and MoO_3–KIT–6 respectively, were assigned to orthorhombic MoO_3 (powder diffraction file #05-0508).

In order to boost the electrical conductivity of the electrode, the mesoporous samples were wrapped by graphene oxide sheets. PDDA polyelectrolyte was added during the synthesis to provide strong electrostatic interaction between the GO support and mesoporous catalysts. In

order to reduce GO to reduced graphene oxide (rGO), the samples were annealed at temperatures of 400 and 600°C under an argon atmosphere. Figure 2 illustrates the XRD patterns of the MoO_3–SBA15 sample composited with both polymer and rGO and annealed at 400 and 600°C, denoted as rGMS-400 and rGMS-600 respectively. Unexpectedly, the XRD patterns indicated that the annealed samples were a mixed phase of partially reduced MoO_3 and a monoclinic phase of MoO_2 (powder diffraction file #73-1807).

Transmission electron microscopy (TEM) analysis revealed that samples preserve the regularity of the template mesostructures (Figure 3). We observe the MoO_3 products have a highly ordered mesostructure throughout the whole domain consisting of hexagonally aligned nanowires and gyroid-porous structures for MoO_3–SBA-15 and MoO_3–KIT-6, respectively, reflecting true replication of the hard templates and a high yield of MoO_3 incorporation into the template channels. N_2 adsorption−desorption isotherms was obtained to examine the textural properties of the catalysts. The prominent hysteresis loops indicate the mesoporous nature of MoO_3–SBA-15 and MoO_3–KIT-6 samples (Figure 3d,e). The Brunauer−Emmett−Teller (BET) surface areas of these catalysts were 50 m^2/g for MoO_3–SBA-15 and 63 m^2/g for MoO_3–KIT-6, all of which were much lower than that for the SBA-15 (529 m^2/g) and KIT-6 (851 m^2/g) templates (see Figure S1 and Table S1, supporting information). The Barrett−Joyner−Halenda (BJH) pore size distributions of MoO_3–SBA-15 and MoO_3–KIT-6 catalysts were centered at 7.2 nm. In the case of MoO_3–SBA-15, the peak at 7.2 nm agrees with that of the original SBA-15 (5.4 nm) and is evidence of well controlled template replication.

Additionally, TEM analysis of rGMS-400 shown in Figure 3c confirmed that thin layers of graphene were attached to the MoO_{3-x} likely as a result of electrostatic interaction. This encapsulation of the mesoporous structure can significantly facilitate the transport of electrons through the highly conductive graphene-based scaffold. Moreover, the conventional (0002) peak expected for graphite at $2\theta = 26.68°$ was not resolved in XRD, which suggests a homogeneous dispersion of the graphene sheets over the surface of the MoO_x samples[27]. The porosity of the rGMS-400 and rGMS-600 composites was quantified using nitrogen adsorption–desorption isotherm measurements (Figure 3f and Table S1, supporting information). According to the BJH equation, the centered pore diameter in rGMS-400 was 7.4 nm, which confirms a relatively uniform pore size distribution. The BET specific surface areas of rGMS-400 and rGMS-600

were 122 and 53 m^2/g, respectively. The higher specific surface area of rGMS-400 compared to MoO_3–SBA-15 (50 m^2/g) is due to the porosity of the replicate MoO_3 and the secondary pores between the MoO_3 and the graphene sheets[18]. The lower surface area of rGMS-600, on the other hand, results from a partial collapse of the mesoporous structure after high temperature reduction at 600°C. TEM and HAADF-STEM images of rGMS-600 (Figure 4) and rGMS-400 (Figure S2, supporting information) catalysts confirm the attachment of mesoporous particles to the rGO. TEM also reveals partial collapse of the porous structures indicated by BET data.

Raman spectra of mesoporous MoO_3–SBA-15 powders and rGMS-400 and rGMS-600 composites is shown in Figure 5. Similar to MoO_3–SBA-15, Raman spectrum of the rGMS-400 composite displayed characteristic orthorhombic MoO_3 vibrational frequencies whereas rGMS-600 peaks are ascribed to Raman bands of monoclinic MoO_2[17] consistent with the XRD analysis. In the MoO_3 spectra, various bending modes were found responsible for the peaks below 400 cm^{-1}, while the three peaks at 663, 820, and 993 cm^{-1} were traced to the various stretching frequencies of molybdenum and oxygen[28]. Raman bands detected at 743, 571, 493, 364, 345 and 229 cm^{-1} in the rGMS-600 sample are the evidence of reduction of MoO_3 to MoO_2[29]. The Raman spectra of the rGMS-400 and rGMS-600 composites in the range of 1200 to 3000 cm^{-1} exhibit the characteristic peaks of rGO. The D and G graphitic bands observed at 1360 and 1594 cm^{-1} for rGMS-400, respectively, and at 1359 and 1583 cm^{-1} for rGMS-600, respectively, confirm the existence of defects in the sp^2-bonded carbon in the composite[30]. The removal of oxygen-containing groups in rGMS-400 and rGMS-600 was monitored by Raman spectroscopy in the range of 1200 to 3000 cm^{-1}. The major oxygen functional groups in GO include epoxide (–O–) and hydroxyl (–OH) groups, which are located on the basal plane of GO, while minor functional groups include carbonyl (–C=O) and carboxyl (–COOH) groups located at the edges[30-34]. GO by itself is known to be electrically insulating due to presence these oxygen groups[35]. Thermal or chemical reduction can remove these groups and restore the electrical properties depending on the degree of reduction, layer disorder, and structural defects[36-38]. The appearance of the defect-induced D-band in the Raman spectra of rGMS-400 at 1360 cm^{-1} as well as a rather broad G-band at 1594 cm^{-1} and unresolved second-order 2D peak (expected ~2700 cm^{-1}) indicated that a high degree of oxidation and disorder[37] was still present in rGMS-400 even though it had been reduced at 400°C (Figure 5b). For rGMS-600, the D-peak shifted to 1359 cm^{-1} and a narrower G-peak at 1583 cm^{-1} was observed. The I_D/I_G ratio decreased from 0.86 for rGMS-400 to 0.19 for

rGMS-600 which indicated that reduction was improved as the annealing temperature was elevated to 600°C. Further reduction of oxygen functional groups in GO by raising the thermal reduction temperature from 400 to 600°C was verified by the high-resolution C 1s spectra acquired from X-ray photoelectron spectroscopy (XPS, shown in Figure 6a). The C 1s spectra of the GMS-400 and GMS-600 composites were deconvolved into four peaks corresponding to carbon atoms with different oxygen-containing functional groups[38]: (1) non-oxygenated C sp^2 and sp^3 at 284.6 and 285.8 eV, respectively, (2) carbon in C–O at 287.4 eV, (3) carbonyl carbon (C=O) at 287.9 eV, and (4) carboxylate carbon (O–C=O) at 289.0 eV. Increasing the intensity of the sp^2 carbon peak relative to the peaks of sp^3 carbon and carbon binding to oxygen indicates a higher degree of reduction by increasing the annealing temperature.

Presence of oxygen vacancy sites (XPS analysis). The presence of oxygen vacancies in the samples was confirmed by XPS analysis (Figure 6b). For the MoO_3–SBA-15 sample, only peaks assigned to Mo^{6+} $3d_{3/2}$ and Mo^{6+} $3d_{5/2}$ at 236.34 and 233.20 eV were detected, respectively. This showed that there were no detectable near-surface oxygen vacancies in MoO_3–SBA-15 and this sample could be regarded as a stoichiometric reference. For rGMS-400 (sampled annealed at 400°C), peaks assigned to Mo^{5+} $3d_{3/2}$ (234.84 eV) and Mo^{5+} $3d_{5/2}$ (231.50 eV) valance states were detected which was an indication of the presence of $v_O^{\cdot}$ vacancy sites ($v_O^{\cdot}$ refers to an oxygen vacancy with a single positive charge according to Kröger-Vink notation). Peaks centered at 232.99 and 229.13 eV were attributed to Mo^{4+} $3d_{3/2}$ and Mo^{4+} $3d_{5/2}$ showing $v_O^{\cdot\cdot}$ oxygen vacancy sites being present with two positive charges. For rGMS-600 (sampled annealed at 600°C), the majority of oxygen vacancy sites were $v_O^{\cdot\cdot}$.

Role of defects in the electrocatalytic reduction of oxygen. The ORR electrocatalytic activity of mesoporous MoO_3–SBA-15, rGMS-400, and rGMS-600 composites were characterized by linear sweep voltammetric (LSV) measurements in 0.1 M KOH and are shown in Figure 7. The activity for MoO_3–KIT-6 is shown in Figure S3, supporting information. The ORR onset potentials of mesoporous MoO_3–SBA-15 and MoO_3–KIT-6 were 0.78 and 0.79 V versus reversible hydrogen electrode (RHE). The improved performance of MoO_3–KIT-6 compared to MoO_3–SBA-15 is assigned to the higher surface area and abundance of three-dimensional channels in the gyroidal structure improving oxygen diffusion on the catalyst surface. Compared with MoO_3–SBA-15,

the rGMS-400 and rGMS-600 electrodes showed an even greater positive shift in the onset potential, 0.82 and 0.86 V (vs. RHE), respectively, with a more notable increase in the current density as shown in Figure 7a. The improved ORR activity of rGMS-400 and rGMS-600 can be explained by following factors. PDDA can functionalize GO through the reduction process and a possible synergic effect between rGO, PDDA, and catalyst plays an important role in high ORR activity of rGMS-400 and rGMS-600. This happens through the physical adsorption of polyelectrolyte chains that contain positively charged nitrogen moieties on rGO where intermolecular charges created a net positive charge on the carbon atoms. This can change the electronic properties of rGO causing the electrons to be attracted more from the anode to the cathode and facilitating oxygen desorption as well as the ORR process[39, 40]. The integration of MoO_3–SBA-15 with PDDA-rGO helps overcome the slow electron conduction in MoO_3–SBA-15 and the interface between them plays a key role in increasing the overall catalytic performance.

Moreover, although the surface area of rGMS-600 (53 m^2/g) was lower than that of rGMS-400 (122 m^2/g), its onset potential (vs. RHE) was 40 mV higher than rGMS-400 at the same mass loading. This higher ORR activity, in spite of having lower surface area, can be attributed to the higher degree of oxygen vacancies on the surface of the active material in the rGMS-600 catalyst due to reduction of orthorhombic MoO_3 to monoclinic MoO_2 by increasing the reduction temperature from 400 to 600 °C accompanied by a higher degree of reduction of GO as confirmed by XPS and Raman spectroscopy.

Electrochemical impedance spectroscopy (EIS) of the catalysts showed smaller diameter of the Nyquist plot curves for rGMS-400, and rGMS-600 compared to MoO_3–SBA-15 (Figure 7b). This is an indication of lower electrical resistance of rGMS-400, and rGMS-600 due to wrapping with more electrically conductive rGO sheets in theses samples. The smaller diameter of the rGMS-600 curve compared to rGMS-400 is due to a combination of the higher oxygen vacancy concentration and a higher degree of reduction of rGO as well as the reduction of the bulk of rGMS-600 from orthorhombic α-MoO_3 to nearly monoclinic MoO_2. Although outside the scope of the current work, the effects of oxygen vacancy concentrations on conductivity can be studied by a set of controlled experiments where the oxygen vacancy concentration is kept as the only

variable in the investigation, most appropriate for single crystalline samples so that the intrinsic contribution of oxygen vacancies to the conductivity can be determined.

Because of its strong orbital overlap[41], MoO_2 has a relatively low, metallic electrical resistivity (8.8×10^{-5} Ω-cm)[16] which can significantly facilitate the electron transfer through the core of catalyst. Accordingly, a comparison between the RDE polarization curves of MoO_3–SBA-15 and rGMS-600 indicates improved the ORR kinetic of rGMS-600 due to this promoted electron conduction the catalyst (Figure 7c,d). The integration of MoO_3 with PDDA-rGO also helps overcome the slow electron conduction in MoO_3–SBA-15. Additionally, in order to reveal the role of the oxygen vacancies on the ORR activity, the LSV of MoO_3–SBA-15 with a sub-stoichiometry degree of $x = 0.024$ was compared with that of as-purchased MoO_3 (Alfa Aesar No. 12930) as a reference sample (denoted as Ref. Alfa Aesar No. 12930) with a slightly higher sub-stochiometry degree of $x = 0.035$[13] (Figure S4, supporting information). The results indicated that the Ref. Alfa Aesar No. 12930 sample was more active than the closer-to-stoichiometric MoO_3–SBA-15 sample by a potential difference of 200 mV (vs. RHE). This was despite the fact that MoO_3–SBA-15 was a mesoporous sample with a high surface area.

In order to model the ORR catalyzed by MoO_{3-x}, the following reaction pathways employed for alkaline solutions[42]:

$$M^{m+}\text{—}O^{2-} + H_2O + e^- \rightarrow M^{(m-1)+}\text{—}OH^- + OH^- \quad (1)$$

$$O_2 + e^- \rightarrow O_{2,ads}^- \quad (2)$$

$$M^{(m-1)+}\text{—}OH^- + O_{2,ads}^- \rightarrow M^{m+}\text{—}O\text{—}O^{2-} + OH^- \quad (3)$$

$$M^{m+}\text{—}O\text{—}O^{2-} + H_2O + e^- \rightarrow M^{(m-1)+}\text{—}O\text{—}OH^- + OH^- \quad (4)$$

$$M^{(m-1)+}\text{—}O\text{—}OH^- + e^- \rightarrow M^{m+}\text{—}O^{2-} + OH^- \quad (5)$$

where M represents the transition metal Mo, *m* denotes the oxidation state, and the subscript "ads" stands for adsorption. In order to identify the ORR active site, DFT calculations based on the above reaction pathways were performed. According to Kim and Dunn *et al.*[43], Mo^{5+} bipolarons and Mo^{4+} polarons at oxygen terminal sites (O_t) are the most favorable defect

configurations with formation enthalpies of 1.32 and 1.51 eV, respectively. The barrier energies against reactions (1), (3), (4), and (5) were calculated by DFT for MoO_3 without oxygen vacancies, and for MoO_{3-x} with a Mo^{4+}-$v_O^{\cdot\cdot}$ surface oxygen vacancy site (Figure 8, Table 1). For reaction (1), barrier energies of 1.54 and 3 eV were significantly reduced to -0.47 and -0.55 eV, respectively, by the presence of the adjacent Mo^{4+}-$v_O^{\cdot\cdot}$ oxygen vacancy site (Figure 8a,b and Table 1). For reaction (3), a similar trend is observed by reducing the energy barriers of 0.471 and 2.053 eV to -1.689 and -1.692 eV, respectively (Figure 8c,d and Table 1). For Reaction (4), the formation of Mo^{5+}─O─OH^- is greatly facilitated by the presence of the surface oxygen vacancy site as the barrier was reduced from 2.158 to -1.410 eV (Figure 8e,f, and Table 1). For Reaction (5), however, the energy barrier against the release of OH^- was slightly increased from 0.739 to 0.968 eV by the presence of the Mo^{4+}-$v_O^{\cdot\cdot}$ vacancy (Figure 8g,h, and Table 1). All the calculated energies were based on the reference states identified in Figure 8. These results agreed with the experimental observations as the rGMS-600 catalyst with the highest degree of metal oxide reduction exhibited the highest ORR activity.

Since durability is a major concern of today's fuel cell industry, the stability of MoO_3–SBA-15 and Pt/C catalysts during ORR were assessed through chronoamperometric measurements at -0.5 V. As shown in Figure S5, supporting information, a relative current of 91% still persisted after 16.7 h on the MoO_3–SBA-15 catalyst. In contrast, Pt/C showed a gradual decrease to 60.0% relative current after only 5.6 h. These results indicate the superior stability of the mesoporous MoO_3–SBA-15 catalyst compared to the Pt/C catalyst in an alkaline solution popular in the development of alkaline fuel cells. On the one hand, Pt-based catalysts gradually degrade over time (especially in alkaline electrolytes) because of surface oxidation, particle dissolution, and particle aggregation. On the other hand, existing ORR catalysts that show improved stability over Pt (such as Ag) still lack the needed activity and are not durable enough for practical purposes[9, 44-46]. The excellent stability and durability of the mesoporous molybdenum oxide even in the absence of rGO protection makes it a promising candidate as a catalyst for ORR.

Conclusion

Reduced graphene oxide-wrapped mesoporous molybdenum oxides were synthesized via a two-step procedure, utilizing nanocasting and a self-assembly/thermal reduction approach, then used

as an electrocatalyst in ORR. The obtained products replicated the mesostructure of both KIT-6 and SBA-15 silica templates and exhibited large surfaces areas (up to 80 m^2/g), and narrow pore size distributions (~3 nm full width at half maximum). The obtained mesoporous MoO_3 material exhibited improved ORR activity, which was associated with the well-defined mesoporous structure. Experimental results indicated that using PDDA for wrapping mesoporous α-MoO_{3-x} with rGO followed with thermal annealing created catalyst surfaces with qualitatively high degree of vacancy densities. Theoretical results have demonstrated that these surface vacancy sites are crucial in the electrochemical activity of catalysts by being the origin of ORR activity in α-MoO_{3-x} based materials for the first time. Finally, we emphasize that the synthesis approach presented here can be readily extended to the preparation of other mesoporous metal oxide–graphene composite materials, with broad applications in various critical energy conversion areas[46]. The calculated results indicated that the energy barriers against ORR were significantly reduced by the presence of Mo^{4+}-$v_O^{\cdot\cdot}$ oxygen vacancy for reactions (1), (3) and (4). The barrier opposing the release of OH^-, given by reaction (5), slightly increased due to the presence of the surface O_t vacancy.

The obtained experimental and computational results demonstrate a pathway for improvement of ORR activity using MoO_{3-x}-based materials, which are known for high thermal stability[13] and electrical conductivity (such as MoO_2)[6]. Future breakthroughs in improving the ORR activity of these materials will be highly impactful due to the rich electrochemical applications enabled by Mo-based metal oxides. For instance, α-MoO_3 is a layered material providing a better access to the crystallographic planes where the reaction occurs. In addition, MoO_3 can be a corrosion-resistant metal oxide, as we have observed stability of the materials even in a strong acid solution such as HF for long periods of several hours. Such properties can have potential applications in chemically-harsh fuel cell environments. Moreover, the synthesis method used in this work for wrapping mesoporous molybdenum oxide with rGO through electrostatic interactions can be used for improving the electrical conductivity of other mesoporous materials when used in composite electrodes. As this study is a first step emphasizing the need for further investigations and advancements on the ORR activity of MoO3 materials, we hope it will inspire future investigations and performance improvements, especially in the computational realm where understanding of descriptors needed for materials design is in a very early stage.

Acknowledgements

Experimental work by R.K.S., S.Y., and M.T.P. was supported by the National Science Foundation under Grant No. CAREER-1553987 (M.T.P., R.K.-S., S.Y.), the UConn Research Foundation, award number PD17-0137 (M.T.P., R.K.-S., S.Y.), and a GE Graduate Fellowship for Innovation (S.Y.). Theoretical and computational work was conducted by T.D.H. and supported by XSEDE through the computational resource allocation number TG-DMR170031. Electrochemical measurements were conducted by Z.C. The authors thank Dr. Roger Ristau for valuable help and discussions on transmission electron microscopy analysis. TEM studies were conducted using facilities in the UConn/FEI Center for Advanced Microscopy and Materials Analysis (CAMMA). This work was partially supported by the Center for Integrated Nanotechnologies, an Office of Science User Facility operated for the U.S. Department of Energy (DOE) Office of Science. Los Alamos National Laboratory, an affirmative action equal opportunity employer, is operated by Los Alamos National Security, LLC, for the National Nuclear Security Administration of the U.S. DOE under contract DE-AC52-06NA25396. The contributions of R.K.-S. and S.Y. are evaluated as equal.

Supporting Information Available: Additional details and discussion of x-ray diffraction (XRD) and specific surface area including table of structural data, transmission electron microscopy (TEM) images and specific surface area analysis of SBA-15 and KIT-6 hard templates, scanning transmission electron microscopy (STEM) analysis of sample rGMS-400, linear sweep voltammetric (LSV) measurements of mesoporous MoO_3–SBA-15 and MoO_3–KIT-6 catalysts, XRD and LSV measurements of MoO_3–SBA-15 and commercially obtained MoO_3 (sample Ref. Alfa Aesar No. 12930), and chronoamperometric response at a potential of -0.5 V *vs.* SCE for mesoporous MoO_3–SBA-15 and Pt/C. This material is available free of charge via the Internet at http://pubs.acs.org.

References

(1) Wagner, F. T.; Lakshmanan, B.; Mathias, M. F. Electrochemistry and the future of the automobile, *J. Phys. Chem. Lett.* **2010**, *1*, 2204–2219.

(2) Yu, W.; Porosoff, M. D.; Chen, J. G. Review of Pt-based bimetallic catalysis: From model surfaces to supported catalysts, *Chem. Rev.* **2012**, *112*, 5780–5817.

(3) Nie, Y.; Li, L.; Wei, Z. Recent advancements in Pt and Pt-free catalysts for oxygen reduction reaction, *Chem. Soc. Rev.* **2015**, *44*, 2168–2201.

(4) Gewirth, A. A.; Thorum, M. S. Electroreduction of dioxygen for fuel-cell applications: Materials and challenges, *Inorg. Chem.* **2010**, *49*, 3557–3566.

(5) Jaouen, F.; Proietti, E.; Lefèvre, M.; Chenitz, R.; Dodelet, J.-P.; Wu, G.; Chung, H. T.; Johnston, C. M.; Zelenay, P. Recent advances in non-precious metal catalysis for oxygen-reduction reaction in polymer electrolyte fuel cells, *Energy Environ. Sci.* **2011**, *4*, 114–130.

(6) Hu, X.; Zhang, W.; Liu, X.; Mei, Y.; Huang, Y. Nanostructured Mo-based electrode materials for electrochemical energy storage, *Chem. Soc. Rev.* **2015**, *44*, 2376–2404.

(7) Chen, Z.; Cummins, D.; Reinecke, B. N.; Clark, E.; Sunkara, M. K.; Jaramillo, T. F. Core–shell MoO_3–MoS_2 nanowires for hydrogen evolution: A functional design for electrocatalytic materials, *Nano Lett.* **2011**, *11*, 4168–4175.

(8) Shi, Y.; Guo, B.; Corr, S. A.; Shi, Q.; Hu, Y.-S.; Heier, K. R.; Chen, L.; Seshadri, R.; Stucky, G. D. Ordered mesoporous metallic MoO_2 materials with highly reversible lithium storage capacity, *Nano Lett.* **2009**, *9*, 4215–4220.

(9) Kim, H.-S.; Cook, J. B.; Lin, H.; Ko, J. S.; Tolbert, S. H.; Ozolins, V.; Dunn, B. Oxygen vacancies enhance pseudocapacitive charge storage properties of MoO_{3-x}, *Nat. Mater.* **2017**, *16*, 454–460.

(10) Chandrasekaran, S.; Kim, E. J.; Chung, J. S.; Bowen, C. R.; Rajagopalan, B.; Adamaki, V.; Misra, R. D. K.; Hur, S. H. High performance bifunctional electrocatalytic activity of a reduced graphene oxide-molybdenum oxide hybrid catalyst, *J. Mater. Chem. A* **2016**, *4*, 13271–13279.

(11) Liang, H.-W.; Wei, W.; Wu, Z.-S.; Feng, X.; Müllen, K. Mesoporous metal–nitrogen-doped carbon electrocatalysts for highly efficient oxygen reduction reaction, *J. Am. Chem. Soc.* **2013**, *135*, 16002–16005.

(12) Guo, S.; Dong, S. Graphene nanosheet: Synthesis, molecular engineering, thin film, hybrids, and energy and analytical applications, *Chem. Soc. Rev.* **2011**, *40*, 2644–2672.

(13) Yazdani, S.; Kashfi-Sadabad, R.; Huan, T. D.; Morales-Acosta, M. D.; Pettes, M. T. Polyelectrolyte-assisted oxygen vacancies: A new route to defect engineering in molybdenum oxide, *Langmuir* **2018**, *34*, 6296–6306.

(14) Sgobba, V.; Guldi, D. M. Carbon nanotubes-electronic/electrochemical properties and application for nanoelectronics and photonics, *Chem. Soc. Rev.* **2009**, *38*, 165–184.

(15) Eder, D. Carbon nanotube−inorganic hybrids, *Chem. Rev.* **2010**, *110*, 1348–1385.

(16) Wang, S.; Yu, D.; Dai, L.; Chang, D. W.; Baek, J.-B. Polyelectrolyte-functionalized graphene as metal-free electrocatalysts for oxygen reduction, *ACS Nano* **2011**, *5*, 6202–6209.

(17) Kim, T.-W.; Kleitz, F.; Paul, B.; Ryoo, R. MCM-48-like large mesoporous silicas with tailored pore structure: Facile synthesis domain in a ternary triblock copolymer−butanol−water system, *J. Am. Chem. Soc.* **2005**, *127*, 7601–7610.

(18) Zhao, D.; Feng, J.; Huo, Q.; Melosh, N.; Fredrickson, G. H.; Chmelka, B. F.; Stucky, G. D. Triblock copolymer syntheses of mesoporous silica with periodic 50 to 300 angstrom pores, *Science* **1998**, *279*, 548–552.

(19) Shi, Y.; Wan, Y.; Zhang, R.; Zhao, D. Synthesis of self-supported ordered mesoporous cobalt and chromium nitrides, *Adv. Funct. Mater.* **2008**, *18*, 2436–2443.

(20) Dickinson, C.; Zhou, W.; Hodgkins, R. P.; Shi, Y.; Zhao, D.; He, H. Formation mechanism of porous single-crystal Cr_2O_3 and Co_3O_4 templated by mesoporous silica, *Chem. Mater.* **2006**, *18*, 3088–3095.

(21) Wang, H.; Cui, L.-F.; Yang, Y.; Sanchez Casalongue, H.; Robinson, J. T.; Liang, Y.; Cui, Y.; Dai, H. Mn_3O_4−graphene hybrid as a high-capacity anode material for lithium ion batteries, *J. Am. Chem. Soc.* **2010**, *132*, 13978–13980.

(22) Hummers, W. S.; Offeman, R. E. Preparation of graphitic oxide, *J. Am. Chem. Soc.* **1958**, *80*, 1339–1339.

(23) Chang, J.; Jin, M.; Yao, F.; Kim, T. H.; Le, V. T.; Yue, H.; Gunes, F.; Li, B.; Ghosh, A.; Xie, S.*, et al.* Asymmetric supercapacitors based on graphene/MnO_2 nanospheres and graphene/MoO_3 nanosheets with high energy density, *Adv. Funct. Mater.* **2013**, *23*, 5074–5083.

(24) Kresse, G.; Furthmüller, J. Efficient iterative schemes for ab initio total-energy calculations using a plane-wave basis set, *Phys. Rev. B* **1996**, *54*, 11169–11186.

(25) Perdew, J. P.; Burke, K.; Ernzerhof, M. Generalized gradient approximation made simple, *Phys. Rev. Lett.* **1996**, *77*, 3865–3868.

(26) Dudarev, S. L.; Botton, G. A.; Savrasov, S. Y.; Humphreys, C. J.; Sutton, A. P. Electron-energy-loss spectra and the structural stability of nickel oxide: An LSDA+U study, *Phys. Rev. B* **1998**, *57*, 1505–1509.

(27) Deskins, N. A.; Dupuis, M. Electron transport via polaron hopping in bulk TiO_2: A density functional theory characterization, *Phys. Rev. B* **2007**, *75*, 195212-1–10.

(28) Yang, S.; Feng, X.; Ivanovici, S.; Müllen, K. Fabrication of graphene-encapsulated oxide nanoparticles: Towards high-performance anode materials for lithium storage, *Angew. Chem. Int. Edit.* **2010**, *49*, 8408–8411.

(29) Yang, X.; Fan, K.; Zhu, Y.; Shen, J.; Jiang, X.; Zhao, P.; Li, C. Tailored graphene-encapsulated mesoporous Co_3O_4 composite microspheres for high-performance lithium ion batteries, *J. Mater. Chem.* **2012**, *22*, 17278–17283.

(30) Dieterle, M.; Mestl, G. Raman spectroscopy of molybdenum oxides Part II. Resonance Raman spectroscopic characterization of the molybdenum oxides Mo_4O_{11} and MoO_2, *Phys. Chem. Chem. Phys.* **2002**, *4*, 822–826.

(31) Sun, Y.; Wang, J.; Zhao, B.; Cai, R.; Ran, R.; Shao, Z. Binder-free α-MoO_3 nanobelt electrode for lithium-ion batteries utilizing van der Waals forces for film formation and connection with current collector, *J. Mater. Chem. A* **2013**, *1*, 4736–4746.

(32) Thomsen, C.; Reich, S. Double resonant Raman scattering in graphite, *Phys. Rev. Lett.* **2000**, *85*, 5214–5217.

(33) De La Cruz, F. A.; Cowley, J. M. Structure of graphitic oxide, *Nature* **1962**, *196*, 468–469.

(34) Cai, W.; Piner, R. D.; Stadermann, F. J.; Park, S.; Shaibat, M. A.; Ishii, Y.; Yang, D.; Velamakanni, A.; An, S. J.; Stoller, M.*, et al.* Synthesis and solid-state NMR structural characterization of ^{13}C-labeled graphite oxide, *Science* **2008**, *321*, 1815–1817.

(35) Lerf, A.; He, H.; Riedl, T.; Forster, M.; Klinowski, J. ^{13}C and ^{1}H MAS NMR studies of graphite oxide and its chemically modified derivatives, *Solid State Ion.* **1997**, *101–103*, 857–862.

(36) He, H.; Klinowski, J.; Forster, M.; Lerf, A. A new structural model for graphite oxide, *Chem. Phys. Lett.* **1998**, *287*, 53–56.

(37) Gao, X.; Jang, J.; Nagase, S. Hydrazine and thermal reduction of graphene oxide: Reaction mechanisms, product structures, and reaction design, *J. Phys. Chem. C* **2010**, *114*, 832–842.

(38) Stankovich, S.; Dikin, D. A.; Piner, R. D.; Kohlhaas, K. A.; Kleinhammes, A.; Jia, Y.; Wu, Y.; Nguyen, S. T.; Ruoff, R. S. Synthesis of graphene-based nanosheets via chemical reduction of exfoliated graphite oxide, *Carbon* **2007**, *45*, 1558–1565.

(39) Mohan, V. B.; Brown, R.; Jayaraman, K.; Bhattacharyya, D. Characterisation of reduced graphene oxide: Effects of reduction variables on electrical conductivity, *Mater. Sci. Eng., B* **2015**, *193*, 49–60.

(40) Tuinstra, F.; Koenig, J. L. Raman spectrum of graphite, *J. Chem. Phys.* **1970**, *53*, 1126–1130.

(41) Fan, Z.-J.; Kai, W.; Yan, J.; Wei, T.; Zhi, L.-J.; Feng, J.; Ren, Y.-m.; Song, L.-P.; Wei, F. Facile synthesis of graphene nanosheets *via* Fe reduction of exfoliated graphite oxide, *ACS Nano* **2011**, *5*, 191–198.

(42) Wang, S.; Yu, D.; Dai, L. Polyelectrolyte functionalized carbon nanotubes as efficient metal-free electrocatalysts for oxygen reduction, *J. Am. Chem. Soc.* **2011**, *133*, 5182–5185.

(43) Spevack, P. A.; McIntyre, N. S. A Raman and XPS investigation of supported molybdenum oxide thin films. 1. Calcination and reduction studies, *J. Phys. Chem.* **1993**, *97*, 11020–11030.

(44) Rogers, D. B.; Shannon, R. D.; Sleight, A. W.; Gillson, J. L. Crystal chemistry of metal dioxides with rutile-related structures, *Inorg. Chem.* **1969**, *8*, 841–849.

(45) Goodenough, J. B.; Cushing, B. L. *Handbook of Fuel Cells–Fundamentals, Technology and Applications*. John Wiley & Sons: New York, **2003**. ISBN: 0-471-49926-9.

(46) Bidault, F.; Brett, D. J. L.; Middleton, P. H.; Brandon, N. P. Review of gas diffusion cathodes for alkaline fuel cells, *J. Power Sources* **2009**, *187*, 39–48.

Figures and Figure Captions

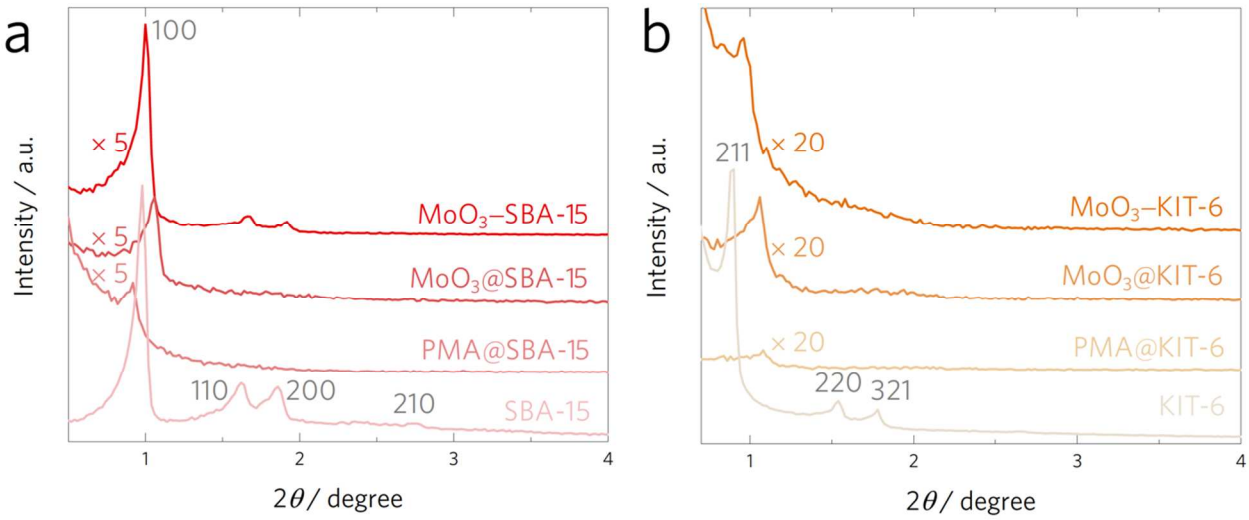

Figure 1. X-ray diffraction (XRD) analysis of the molybdenum oxide hard templating process. (a) Low-angle powder XRD of the mesoporous silica KIT-6 hard template, the mesostructured composite of phosphomolybdic acid (Mo precursor) impregnated into the SBA-15 mesochannels (PMA@SBA-15), the mesostructured MoO_3@SBA-15 composite prepared via high-temperature calcination of PMA@SBA-15 in air at 600°C, and the final product of mesoporous MoO_3 after removal of the SBA-15 hard template by hydrofluoric acid (MoO_3–SBA-15). (b) Low-angle powder XRD of KIT-6, PMA@KIT-6, MoO_3@KIT-6, and the mesoporous MoO_3–KIT-6 sample after removing the template.

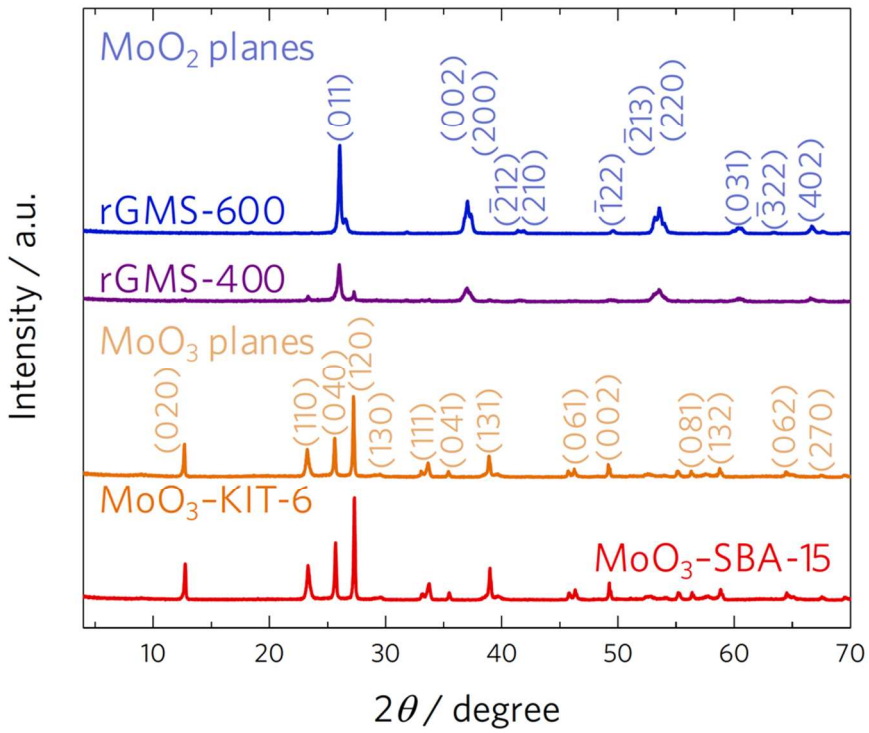

Figure 2. High-angle powder XRD patterns of the mesoporous MoO_3–SBA-15 and MoO_3–KIT-6 samples. The patterns are assigned to an orthorhombic phase of MoO_3 (powder diffraction file #05-0508). High-angle powder XRD patterns of the composites with MoO_3–SBA-15, PDDA polyectrolyte, and rGO annealed at 400 and 600°C under argon, denoted as rGMS-400 and rGMS-600 respectively. The patterns are assigned to the monoclinic phase of MoO_2 (powder diffraction file #73-1807).

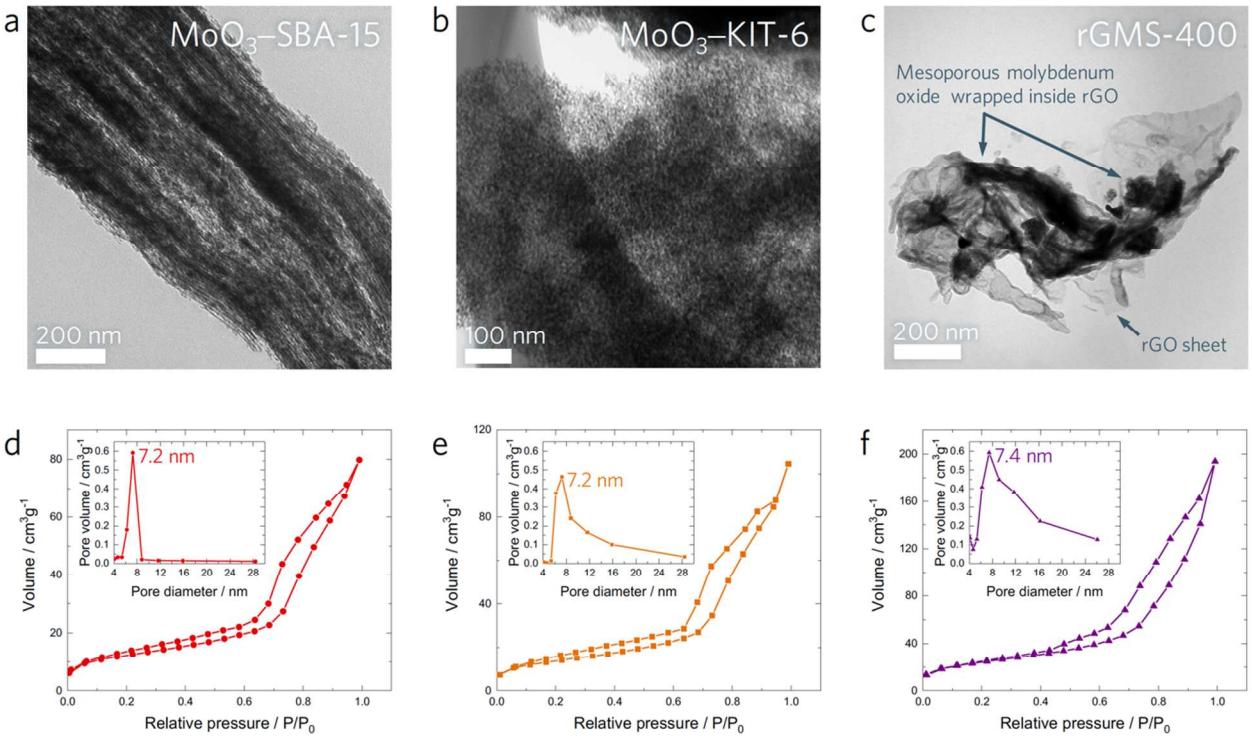

Figure 3. Transmission electron microscopy (TEM) analysis of mesoporous MoO_3 and composite catalysts. TEM images of (a) MoO_3–SBA-15, (b) MoO_3–KIT-6, and (c) rGMS-400. (d−f) Corresponding N_2 adsorption isotherm curves for the three mesoporous MoO_3 catalysts shown in panels (a–c). Insets show the calculated Barrett−Joyner−Halenda pore size distributions.

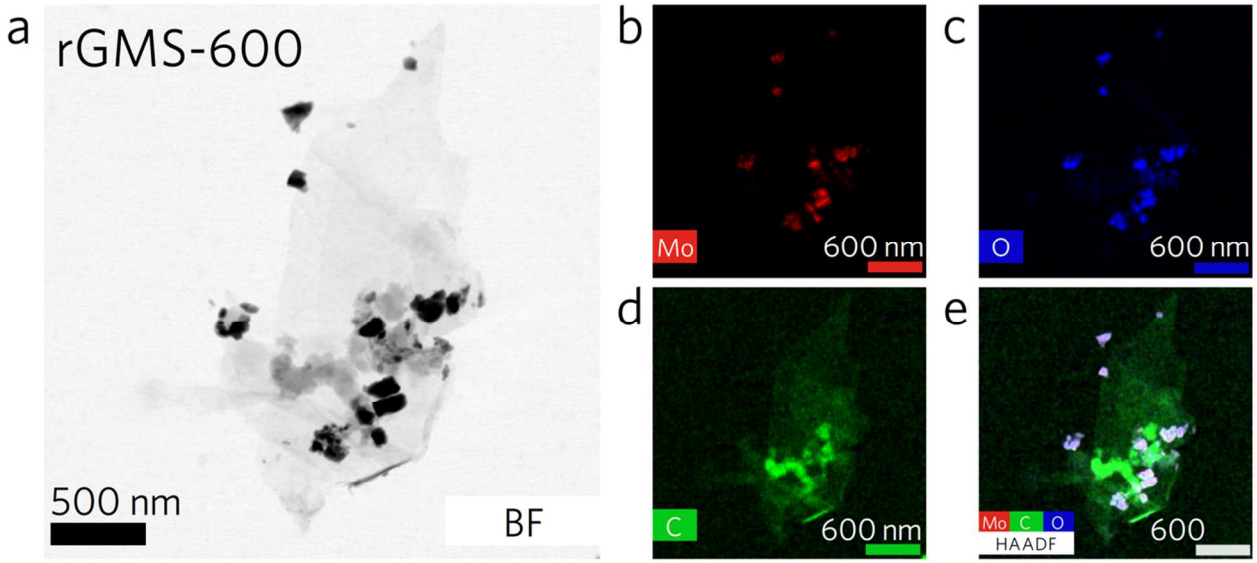

Figure 4. Scanning transmission electron microscopy (STEM) confirms wrapping of MoO_{3-x} catalysts by rGO. (a) Bright field STEM and (b-e) scanning energy dispersive X-ray spectroscopy (EDS) and high angle annular dark field (HAADF) micrographs of rGMS-600.

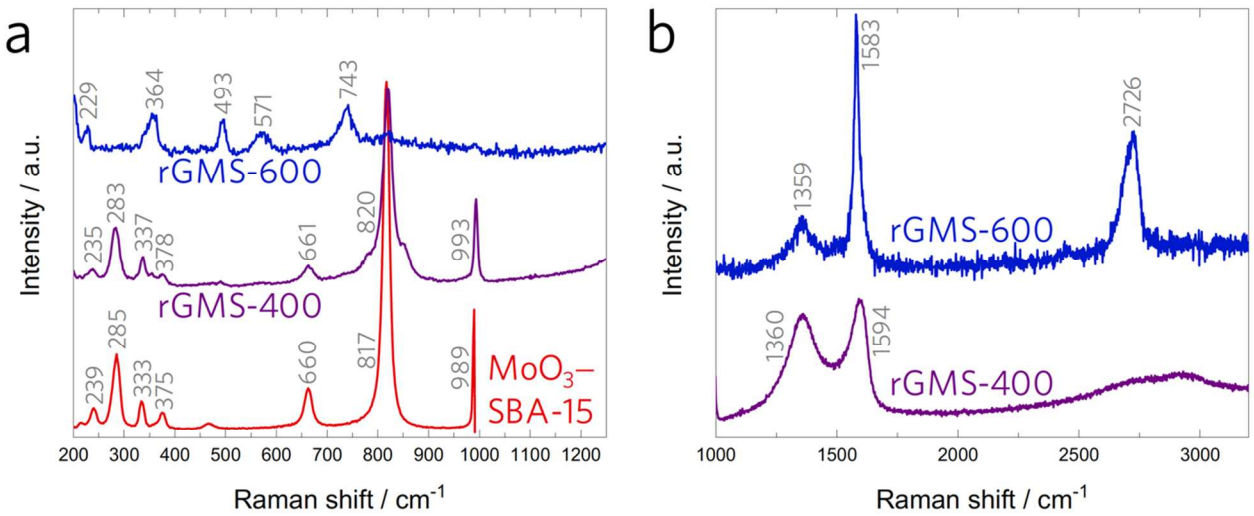

Figure 5. (a) Raman spectra of rGMS-400 and rGMS-600 composites shown in comparison with that of mesoporous MoO_3–SBA-15. (b) Raman spectra of the rGO-related peaks of rGMS-400 and rGMS-600 samples.

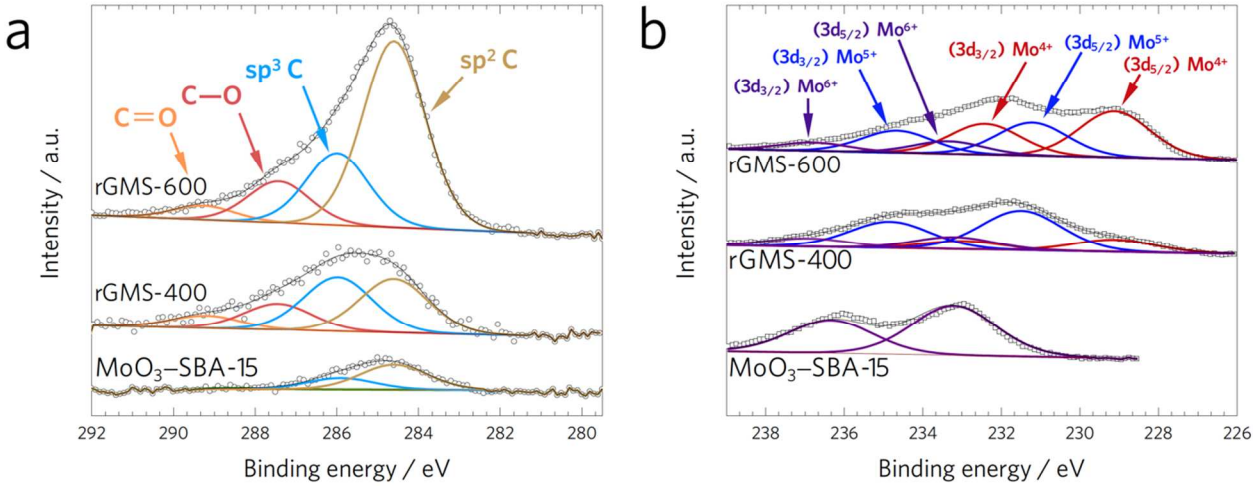

Figure 6. (a) *Deconvoluted XPS carbon 1s peak of MoO_3–SBA-15 and the rGMS-400 and rGMS-600 composites. (b) XPS analysis illustrating the presence of Mo^{5+} and Mo^{4+} valance states corresponding to $v_O^{\cdot}$ and $v_O^{\cdot\cdot}$ oxygen vacancy sites, respectively, in both samples rGMS-400 and rGMS-600°C. For MoO_3–SBA-15 only Mo^{6+} peaks were detected indicating the sample being fully-oxidized.*

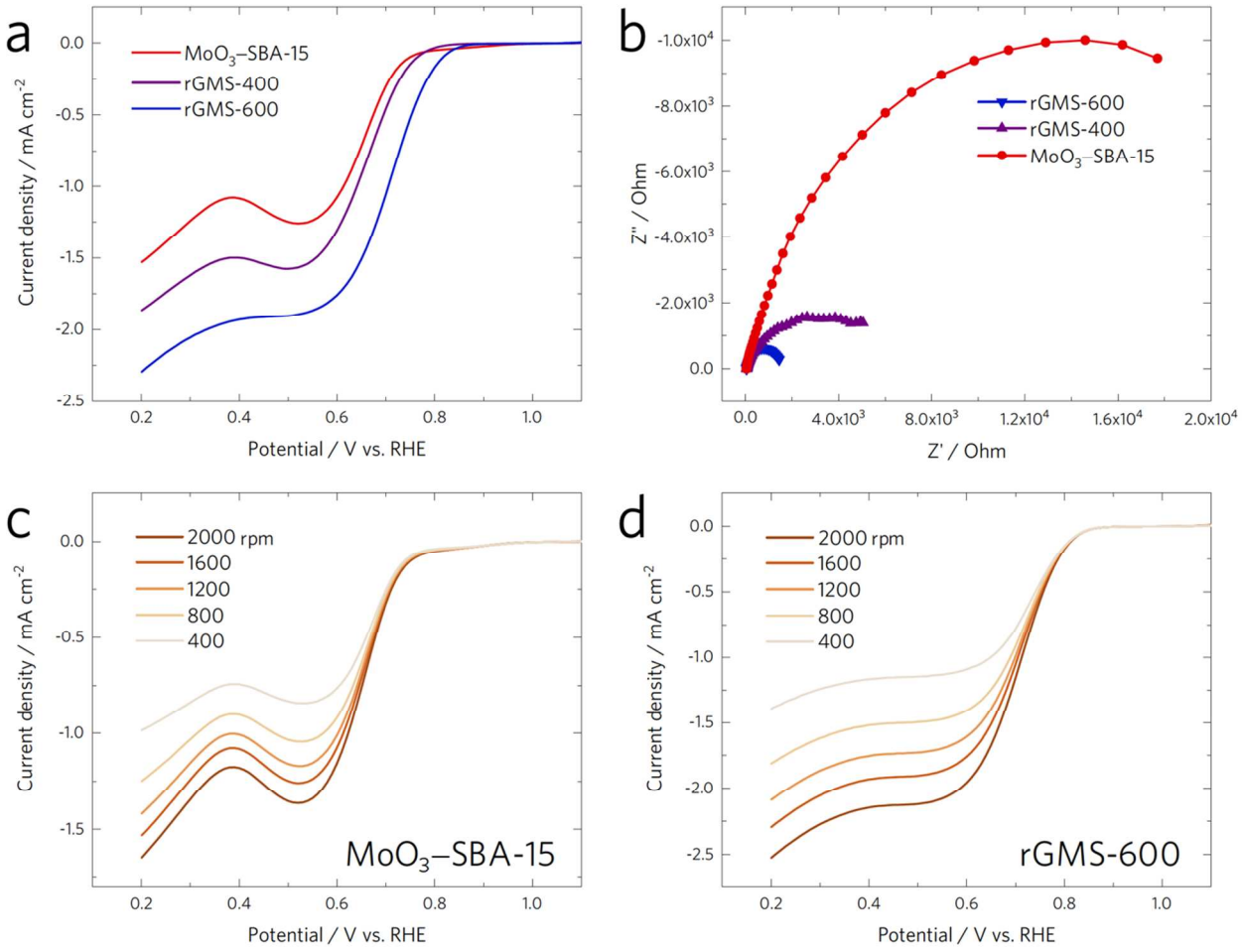

Figure 7. Oxygen reduction activity is increased through a composite electrode with less defective rGO and more highly reduced MoO_{3-x}, demonstrating the importance of PDDA and thermal treatment at 600°C. (a) Linear sweep voltammetry polarization curves obtained in O_2-saturated 0.1 M KOH and (b) Nyquist plots for MoO_3–SBA-15, rGMS-400, and rGMS-600 catalysts. Rotating-disk voltammograms of the catalysts: (c) MoO_3–SBA-15 and (d) rGMS-600 in O_2-saturated 0.1 M KOH with a sweep rate of 5 $mV \cdot s^{-1}$.

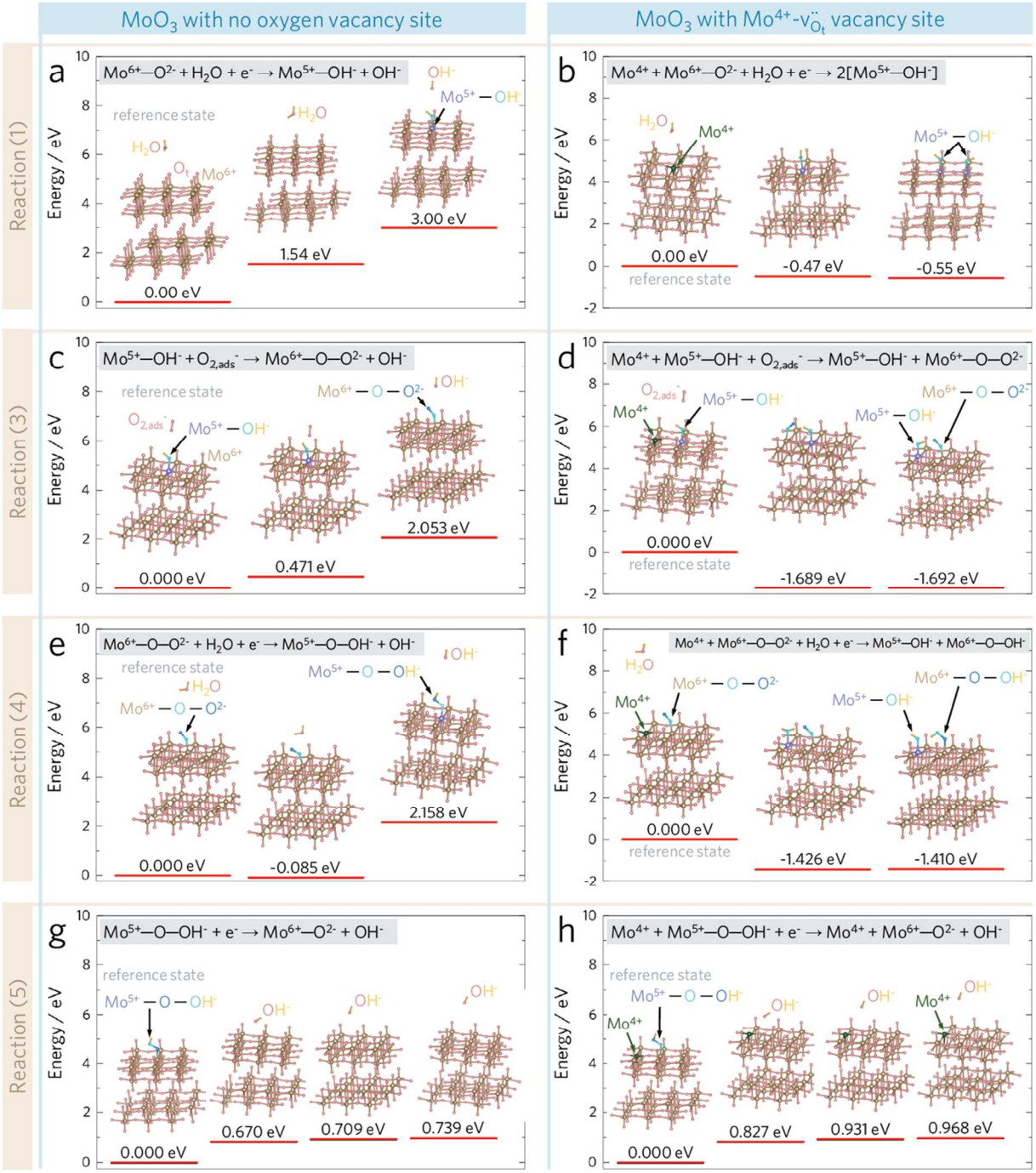

Figure 8. The effect of a surface oxygen vacancy site on the energy barriers for ORR. DFT calculated energy barriers for the oxygen reduction reaction (ORR) with a MoO_3 catalyst: (a,c,e,g) with no oxygen vacancy, and (b,d,f,h) with the presence of a Mo^{4+}-$v_O^{\cdot\cdot}$ surface oxygen vacancy site. The performed calculations show that the energy barriers of ORR kinetics are significantly reduced due the presence of the surface oxygen vacancy (a,b) based on reaction (1),

(c,d) based on reaction (3), and (e,f) based on reaction (4). (g,h) The presence of the oxygen vacancy site slightly increases the barrier energy against the reduction of Mo^{5+}─O─OH^- and release of OH^- according to reaction (5). In these calculations, the products and reactants are conserved, which is required to enable direct comparison between the different states.

Table 1. Proposed reaction pathways, and their DFT calculated energy barriers for oxygen reduction reaction activity of MoO_3, and MoO_{3-x} with a Mo^{4+}–O_t vacancy site on the surface.

Reaction	Proposed reaction pathway to create MoO_3 with no oxygen vacancy	Energy barrier (eV) at each step	Proposed reaction pathway to create MoO_3-Mo^{4+}□O_t vacancy	Energy barrier (eV) at each step
(1)	Mo^{6+}─O^{2-} + H_2O + e^- → Mo^{5+}─OH^- + OH^-	1.54 eV 3 eV	Mo^{4+} + Mo^{6+}─O^{2-} + H_2O + e^- → 2[Mo^{5+}─OH^-]	-0.47 eV -0.55 eV
(3)	Mo^{5+}─OH^- + $O_{2,ads}^-$ → Mo^{6+}─O─O^{2-} + OH^-	0.471 eV 2.053 eV	Mo^{4+} + Mo^{5+}─OH^- + $O_{2,ads}^-$ → Mo^{5+}─OH^- + Mo^{6+}─O─O^{2-}	-1.689 eV -1.692 eV
(4)	Mo^{6+}─O─O^{2-} + H_2O + e^- → Mo^{5+}─O─OH^- + OH^-	-0.085 eV 2.158 eV	Mo^{4+}+Mo^{6+}─O─O^{2-} + H_2O + e^- → Mo^{5+}─O─OH^- + Mo^{6+}─O─OH^-	-1.426 eV -1.410 eV
(5)	Mo^{5+}─O─OH^- + e^- → Mo^{6+}─O^{2-} + OH^-	0.670 eV 0.709 eV 0.739 eV	Mo^{4+}+Mo^{5+}─O─OH^- + e^- → Mo^{4+}+Mo^{6+}─O^{2-} + OH^-	0.827 eV 0.931 eV 0.968 eV

TOC Graphic

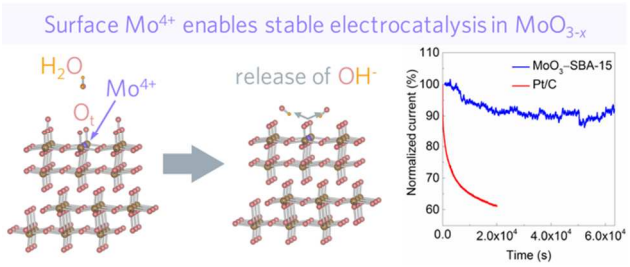
Surface Mo4+ enables stable electrocatalysis in MoO3-x
H2O
Mo4+
Ot
release of OH-
MoOx-SBA-15
Pt/C
Normalized current (%)
110
100
90
80
70
60
0.0
2.0x10^4
4.0x10^4
6.0x10^4
Time (s)